Title: Energy absorption analysis of aramid composite during blunt projectile impact

Authors: Ignacio Rubio Díaz - Marcos Rodríguez Millán - A. Rusinek - María Henar Miguélez Garrido - José Antonio Loya Lorenzo

Version of record available online at
https://doi.org/10.1080/15376494.2021.1963020

Energy absorption analysis of aramid composite during blunt projectile impact.

I. Rubio[a], M. Rodríguez-Millán [a], A. Rusinek [b], M.H. Miguélez [a], J.A. Loya [c*]

[a] *Department of Mechanical Engineering, University Carlos III of Madrid, Avda. de la Universidad 30, 28911, Leganés, Madrid, Spain*
[b] *Laboratory of Microstructure Studies and Mechanics of Materials (LEM3), Lorraine University, 7 rue Félix Savart, BP 15082, 57073 Metz CEDEX 03, France*
[c] *Department of Continuum Mechanics and Structural Analysis, University Carlos III of Madrid, Avda. de la Universidad 30, 28911 Leganés, Madrid, Spain*

** corresponding author*
Email address: jloya@ing.uc3m.es
Phone number: +34 916248880

Abstract

In this work, a numerical model for aramid composites is experimentally validated in terms of permanent deformation, energy absorption and damage mechanisms for ballistic applications. Novel experimental and numerical results of non-perforating ballistic impacts with blunt projectiles are presented. The resistance forces and absorption energy by the specimen are measured for different impact velocities. A post-mortem analysis of the failure mechanisms is performed using computed tomography and a profilometer device. The numerical model is used to analyse the influence of impactor mass and impact velocity below the ballistic limit.

Keywords: Aramid composite, blunt projectile, resistance force, delamination, impact, finite element, energy absorption

1. Introduction

The woven aramid prepreg materials are widely used to construct protective structures, such as combat helmets and vehicle armor, due to their combination of high specific stiffness and strength [1]. The analysis of these structures under ballistic impact at high impact velocities involves perforation and/or non-perforation tests. Generally, tests performed by manufacturers and developed according to standards for the design of protections are focused on non-perforation. The main standard for non-perforation analysis of armour, like combat helmets, is NIJ 0101.06 [2], which involves using 9×19 mm FMJ (Full Metal Jacketed) projectiles. The trauma generated during the impact event is measured using Roma nº1 ballistic plasticine. However, the main studies related to the analysis of laminated aramid's mechanical behaviour have been carried out on perforation [3–6]. The lack of studies on non-perforation testing difficult the development of numerical tools for protections designing, since validation should be carried out in these conditions.

Tan et al. [3] developed experimental tests and numerical simulations with projectiles of different nose shape to obtain the ballistic limit, the absorption energy and the penetration failure mechanisms. Similarly, Bresciani et al. [4] developed an experimental and numerical study of perforation impacts with blunt projectiles in which the impact angle and the subsequent delamination after impact were analysed. Post-mortem analysis was performed by cross-sectioning the specimens. Li et al.[5] studied the influence of the blunt projectile material on the deflection of aramid composite plates. They used steel and aluminium foam blunt projectiles. The main mode of impact kinetic energy dissipation was by deforming the aluminium foam projectile. However, energy dissipation was carried out in the aramid plate using the steel projectile. Wang et al. [6] experimentally analysed the ballistic behaviour of Kevlar/epoxy specimens of different thicknesses using projectiles of different geometries, including the blunt-type projectile. From each test, the influence of the projectile geometry in terms of absorbed energy was analysed and related to the degree of damage induced to the specimens. Sikarwar et al [7] in their experimental work on the impact of 9 mm FMJ projectiles on laminates of different Kevlar/epoxy stacking orientations performed an analytical study of the energy balance absorbed during impact.

Due to the high porosity of aramid laminates, the most commonly used methods for damage detection in this type of composite material are the visual inspection of the specimen and cutting it in the half to evaluate the morphology of the different failure modes [8-15]. However, Computed Tomography (CT) is a technique that does not require the destruction of the specimen and allows knowing the extension of the delaminated area or its qualitative study [16-20].

In a previous work [6], different technologies effectiveness to assess aramid composites after ballistic impact was evaluated. Computed Tomography (CT) and force sensors were used to record the delamination and impact force; the permanent residual deformation was measured with a profilometer device. The method's effectiveness was evaluated for the impact of conical and blunt projectiles above the ballistic limit.

The present work focuses on the analysis of the aramid composite under high energy impact loads in non-perforating conditions. This analysis is relevant for manufacturers because these conditions are common during the service life of combat helmets. Non-perforation velocities can cause stiffness losses and reduce its structural performance. For this study, an analysis of the resistant force of the material for different impact energies was carried out. Moreover, a study of the remaining deformation in the material after impact is performed by profilometry. Computerized tomography was used to analyse the damage in the specimen after impact. This novel experimental methodology constituted the basis for the calibration/validation of the numerical model. The numerical model allowed to analyse the internal energies, the influence of projectile velocity on resistance force and the influence of the projectile mass for impact velocities not achieved experimentally.

2. Experimental set-up

2.1. Material plates

The specimen consists of flat plates of aramid composite, in particular K129 fibres embedded in Polivynil Butyral Phenolic matrix (PVB). Each layer presents a plain wave woven configuration of fibres. The manufacturing of the plates consists of hand-made stacking of the different layers (woven fibres and matrix), and then hot-pressing is applied in order to provide the material with the necessary cohesion to stiff the plate. The dimensions of the plate are $130x130\ mm^2$ with an areal density of 8.86 kg/m^2, units typically used in personal protection design to define the thickness of the sample.

2.2. Ballistic impact device

Ballistic impact tests are carried out using a pneumatic gas gun to launch a blunt projectile orthogonal to the composite plate. The diameter of the gas gun barrel is 13 mm, roughly equal to the projectile diameter, to avoid sabot and not include extra damage by the sabot in the specimens. The initial impact velocity (V_o) can be adjusted by changing the gas pressure in the tank, P_0.

A set-up of laser sensor is used to measure the initial impact velocity of the projectile (V_o). They are fixed at the exit of the barrel, perpendicular to the projectile trajectory. The impact velocity is defined as $V_o = \Delta X^{laser}/\Delta time$, where $\Delta time$ is the interval rise time when the projectile crosses from the first to the second laser beam, and ΔX^{laser} is the distance between both laser beams, $\Delta X^{laser} = 5\ cm$.

A schematic description of the set-up and sensors position is described in Figure 1.

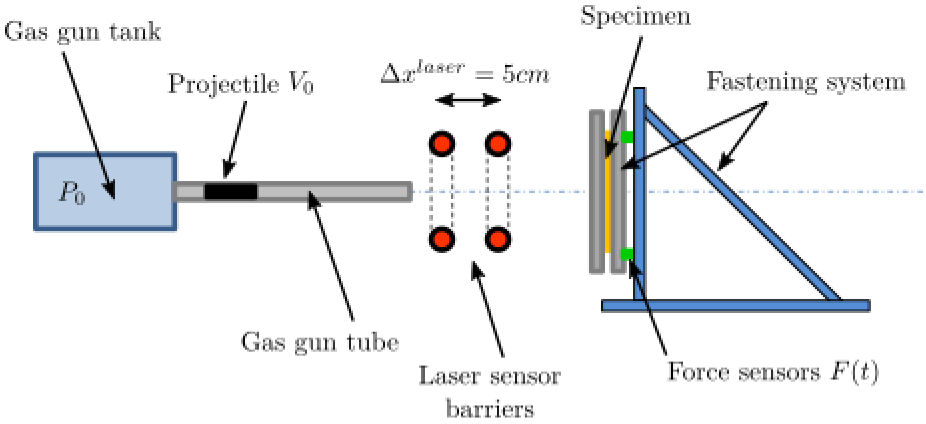

Figure 1. Experimental set-up of devices used on the impact test.

The composite plates (130 x 130 mm^2) are embedded by two steel frames forming a fastening system, resulting in an effective area of 100 × 100 mm^2 (Figure 2a).

The projectile is made of heat-treated *maraging* steel with a hardness close to 640HV and a yield stress of $\sigma_y \approx 2GPa$. Blunt nose shape projectile with a diameter of 13 mm, a length of 29 mm and a mass of 28.9 g. is used during all the tests performed [21] (Figure 2b).

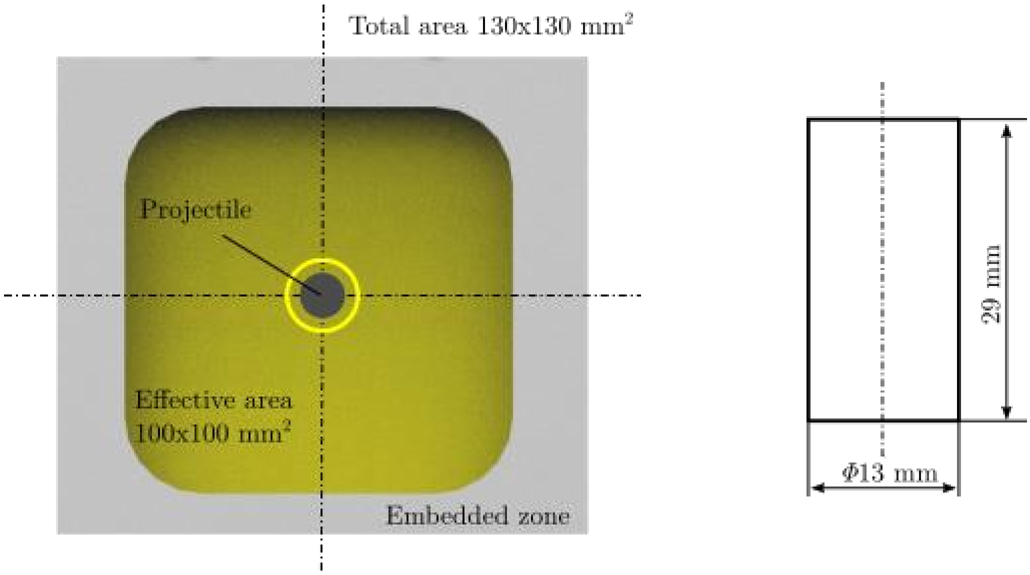

a) b)

Figure 2. Dimensions of the target and the projectile used in tests. (a) Target geometry. (b) Projectile shape and dimensions

A force sensor set composed of four individual piezoelectric sensors is installed to measure the overall resistance force history *F(t)*. The sensors are fixed on the back face of the target holder and the fastening plate device, Fig. 1. The sensors (9011A Kistler) are used to measure only the uniaxial dynamic load along the impact direction. The maximum force on the specimen that can be measured is the sum of each sensor's individual and varies from 60 to 80 *kN* [20,21]. Each sensor has a natural frequency of 65 *kHz,* and it can measure a wide range of forces from 0 to 15 *kN* with a tolerance is ± *5kN*. Figure 3 shows the sensor location on the impact device. Similar studies about resistance force using a similar experimental device have been described in the literature when testing other materials [22,23]

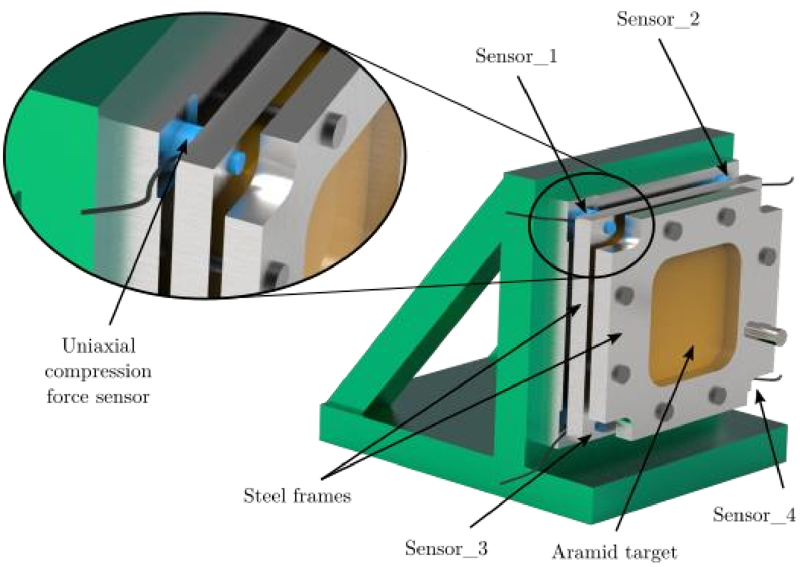

Figure 3. Fastening target plate and measurement system location.

In addition to the analysis of the mechanical behavior of the composite, a systematic study of the impacted plates has been performed to estimate the damage in the samples due to the impact event.

2.3. Post-morten deformation (PBFD)

A *MahrSurf* model *CD 120* digital profilometer is used to obtain the permanent back-face deformation (PFBD) on plates (Figure 4). The profilometer uses a needle with a radius of 20 μm and an arm of 350 *mm*. The precision obtained during measurements is related to the radius of the touch probe needle. The needle goes through the rear profile of the plate in the zenith plane. A set of coordinates of the profile points is obtained using *Mahr Easycontour* software, which allows to measure the maximum value of back face deformation of each tested sample. This method allows to obtain the permanent deformation (PBFB) induced in the specimen in a precise way for further comparison with numerical predictions.

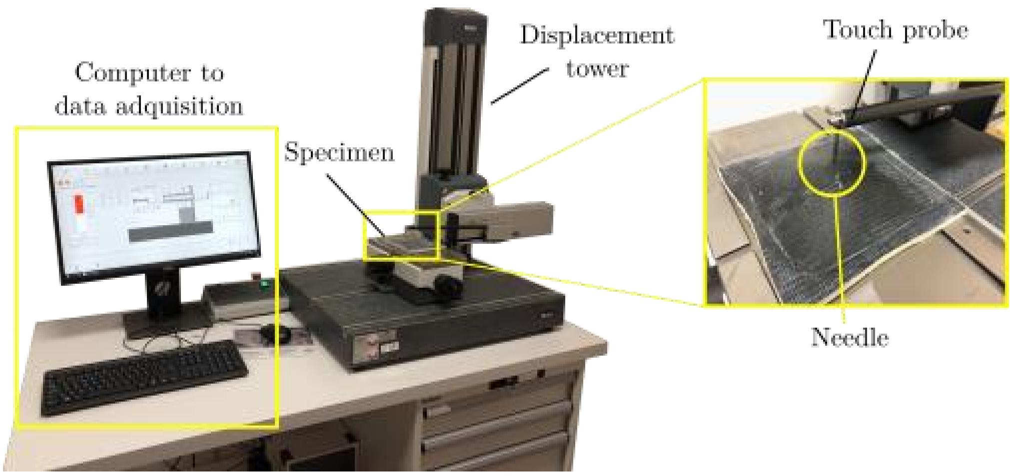

Figure 4. Profilometer device to measure the permanent back face deformation.

In addition to induced damage observed externally on specimens, internal damage occurs due to delamination, shear failure or compression layers. In order to avoid introducing additional damage in the specimen by cutting process that may affect the morphology of the failure modes observed, a non-destructive damage analysis technique (X-ray-based computed tomography) is used. The following section describes this technique, which allows qualitative analysis of internal damage in specimens.

2.4. CT-Scan for tomography

An analysis of the internal damage of the plates after impact is carried out by tomography of post-mortem specimens. All Images are obtained by X-ray microtomography device (EasyTom Nano, Rx Solutions) with a minimum X-ray beam power of 160 kW and a precision of $0.5\mu m$. The analysis of each plate requires around 4 hours. AVIZO and X-Act 2.0 software for processing images from tomography are used. With this technique, it is possible to analyse internal damage induced in the plates due to impact without the necessity of destroying the specimen, i.e., with middle cutting.

3. Numerical simulation

The numerical model is developed in the FEM software Abaqus/Explicit 6.17. Aramid composite material behaviour is defined through a user subroutine VUMAT that considers the anisotropy of the composite material.

The numerical model is composed of different parts: the aramid plate, the blunt projectile, the auxiliary steel frames where the specimens are embedded, cylinder-shaped sensors, and different screws to fasten and fix all the parts [22]. The material models, geometries, boundary conditions and mesh, are defined below. A quarter-symmetry mesh is developed to reduce the computational time.

3.1. Aramid composite plates

3.1.1. Mechanical behaviour of aramid/PVB laminates

The mechanical behaviour of the aramid composite plate is assumed as an orthotropic elastic material up to failure. This approach is widely used for composite models using impact problems [9,10,16,22-24]. The mechanical properties of the aramid composite used in this study are shown in Table 2.

The failure model distinguishes between intra-laminar failure and inter-laminar failure or delamination.

- Intra-laminar failure

The mechanical behaviour of each layer of aramid composite is assumed as linear elastic until failure. The failure is predicted using a modification of the Hou et al. failure criteria [15], equations 1-3, through a VUMAT user subroutine. The criterion is formulated based on in-plane and out-of-plane stress distribution. This model has been previously successfully applied in previous work [17]. The stress distribution for in-plane and out-of-plane failure modes is shown in Figure 5.

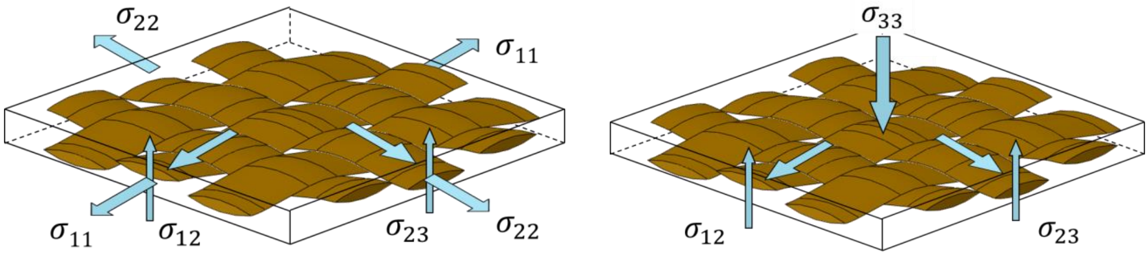

a) b)

Figure 5. Stress components distribution involved in each failure mode. a) In plane tension distribution. b) Out of plane tension distribution.

The failure model is described in the following part depending on the loading direction.

- In-Plane failure modes

Fibre failure in direction 1

$$d_{f1} = \left(\frac{\sigma_{11}}{X_{1T}}\right)^2 + \left(\frac{\sigma_{12}}{S_{12}}\right)^2 + \left(\frac{\sigma_{13}}{S_{13}}\right)^2 \quad 1)$$

Fibre failure in direction 2

$$d_{f2} = \left(\frac{\sigma_{22}}{X_{2T}}\right)^2 + \left(\frac{\sigma_{12}}{S_{12}}\right)^2 + \left(\frac{\sigma_{23}}{S_{23}}\right)^2 \quad 2)$$

Where σ_{11}, σ_{22} correspond with stresses in fibre direction (1 and 2) respectively; σ_{12}, σ_{23}, and σ_{13} are the shear stresses; X_{1T}, X_{2T} threshold stresses in the fibre direction and, finally, S_{12}, S_{23} and S_{13} are the transverse shear strengths.

- Out-of-Plane failure modes

Failure in direction 3

$$d_{f3} = \left(\frac{\sigma_{33}}{Z_c}\right)^2 + \left(\frac{\sigma_{13}}{S_{13}}\right)^2 + \left(\frac{\sigma_{23}}{S_{23}}\right)^2 \quad 3)$$

Where σ_{33} and Z_c are the stress and strength in through-thickness direction, σ_{23}, and σ_{13} are the shear stresses and S_{23} and S_{13} are the transverse shear strengths.

Matrix failure is not considered due to the low resin content in the composite, about 18%. The main failure mode is the fibre failure along each direction (eqs. 1-3). All mechanical properties of aramid composite are presented in table 2.

E_1 (GPa)	E_2 (GPa)	E_3 (GPa)	G_{12} (GPa)	G_{13} (GPa)	G_{23} (GPa)	ν_{12} (-)	ν_{13} (-)	ν_{23} (-)	ρ (kg/m^3)
22.0	22.0	9.0	0.77	5.34	5.34	0.25	0.33	0.33	1230

S_{1t} (MPa)	S_{1c} (MPa)	S_{2t} (MPa)	S_{2c} (MPa)	S_{3t} (MPa)	S_{3c} (MPa)	S_{12} (MPa)	S_{13} (MPa)	S_{23} (MPa)
800	80	800	80	1200	1200	77	898	898

Table 2. Mechanical properties of aramid composite [26].

Failure is considered when any damage variable "d_i" $(i = f1, f2, f3)$ is equal to 1. At this time, the stresses involved in damage criteria (eqs. 1-3) are set to zero. Furthermore, it produces large deformations and distorted elements in the model, which do not contribute to the strength and stiffness of the laminate, but can produce loss of convergence during simulations and instability. Thus, it is necessary to include deletion criteria of distorted elements based on maximum deformation using a VUMAT subroutine. Before calculating each time increment, the strains in different directions were evaluated by comparing them to a critical value. This method for simulating failure has been reported in previous works [13,17,24,29].

- Inter-laminar failure

Interlaminar failure of the composite is modelled using cohesive surfaces. The damage initiation criteria and its evolution define cohesive interlaminar behaviour. The use of cohesive surfaces instead of cohesive elements presents some advantages: it improves the computational cost without adding mass or stiffness to the model.

The model used in this work is based on the traction-separation law, and it assumes a linear elastic behaviour, followed by damage initiation criteria and a damage evolution law describing the cohesive stiffness degradation mode. The damage evolution is described as a non-linear evolution law once the initiation criteria are reached.

The damage initiation criterion is based on stresses in a quadratic form (eq. 4)

$$\left(\frac{t_n}{t_n^0}\right)^2 + \left(\frac{t_s}{t_s^0}\right)^2 + \left(\frac{t_t}{t_t^0}\right)^2 \geq 1 \qquad 4)$$

Where (t_n^0) is the normal threshold stress and t_s^0, t_t^0 are the shear strengths, respectively, and their values are listed in table 3.

G_n^c (J/mm^2)	$G_t^c = G_s^c$ (J/mm^2)	t_n^0 (MPa)	$t_t^0 = t_s^0$ (MPa)	α
0.24	0.47	34.5	9.0	1

Table 3. Cohesive properties used in the numerical model.

The damage evolution law is based on mix-mode fracture energy. That energy is the area under the traction-separation curve [30]. The damage evolution criterion implemented in this work is based on a potential law based on energies (eq. 5)

$$\left(\frac{G_n}{G_n^c}\right)^{\alpha} + \left(\frac{G_s}{G_s^c}\right)^{\alpha} + \left(\frac{G_t}{G_t^c}\right)^{\alpha} = 1 \qquad 5)$$

where G_n, G_s and G_t are, respectively, the released rate energies in normal and shear directions, G_n^c, G_s^c and G_t^c are the corresponding critical values and, α is a parameter model.

3.1.2. Modelling of aramid/PVB laminates

The plate is meshed with 8-node hexahedral elements of with reduced integration (C3D8R). Each plate contains 8952 elements with 18234 nodes. One element per layer through-thickness is used to mesh the plate. The mesh structure is divided into a central area and the rest of the plate. The central area dimensions are 15 × 15 mm^2 -twice the projectile diameter-; the mesh is refined and structured in this area to define the damage zone with precision. The element size with an aspect ratio of 1.62 is used. Out of this region, the element size increases up to 1 mm, with an unstructured mesh. (Figure 6). A mesh sensitivity analysis is carried out to minimise the error in the results obtained and the computational time.

3.2. Projectile

The projectile is modelled as a linear elastic solid because no plastic deformation is observed after impact tests. This assessment allows to reduce the computational time during simulations. The dimensions of the projectile are the same as used during experiments. An equivalent density is defined to provide the projectile with the exact mass of 28.9 g. The projectile density is set to $\rho_{eqv} = 7744\ kg/m^3$. The mesh of the projectile consists of 2400 elements and 2944 nodes for the quarter of geometry simulated.

3.3. Target holder

According to the experimental set-up, the target holder is modelled as two steel frames (front and rear holders). Each frame dimensions are 190 × 180 × 15 mm^3 with an effective area of 100 × 100 mm^2. The target holder is modelled as a linear elastic solid with 8-nodes hexahedral elements and reduced integration. The mesh density varied from fine to coarser from the sensor zone to the outer periphery of the for accurate impact force measurement results.

To ensure that both steel frames do not separate and obtain a correct record of the evolution of the resistant force during the impact, the steel frames were joined using two screws modelled as linear elastic. The screws were fastened to the frames, modelled by TIE type joints. The dimensions of the screw are $\Phi = 10\ mm$ and $h = 13\ mm$, and are meshed with 8-nodes hexahedral elements with reduced interaction.

3.4. Sensors modelling and description.

The sensor is modelled as linear elastic behaviour because no plastic deformations are observed after impacts. The dimensions of the sensor are $\Phi = 5\ mm$ and $h = 5\ mm$. They are meshed with 8-nodes hexahedral elements with reduced integration.

In the experimental case, the cylinder-shaped sensors (in blue in Figure 3) are fasten to the supporting rig (in green in Figure 3). Therefore, these sensors define 4 point boundary conditions for the steel frame. According to the impact energy, steel frame stiffness, etc., it could affect the reaction forces appearing during the impact in a general case, so they modelled according to the experience depicted in previous papers [22,23]

Numerically, sensors are modelled in a simplified way as a cylindrical tip on the steel frame at the sensor location. The end of the sensor connects to the green rig, where the reaction force is measured, is modelled as an encastred surface. The 4 reaction forces were experimentally measured and compared at the corresponding numerical at the same points.

Moreover, numerical screws are modelled as simplified steel cylinders of equivalent diameter and stiffness, just connecting rear and front frames to keep the specimen supported in the perimeter. A friction coefficient of 0.2 between specimen and frame has been considered. The qualitative comparison of experimental and numerical specimen after impact (see Figure 9) show a very similar deformed shape.

The numerical set-up for impact testing in ABAQUS/Explicit can be observed in Figure 6.

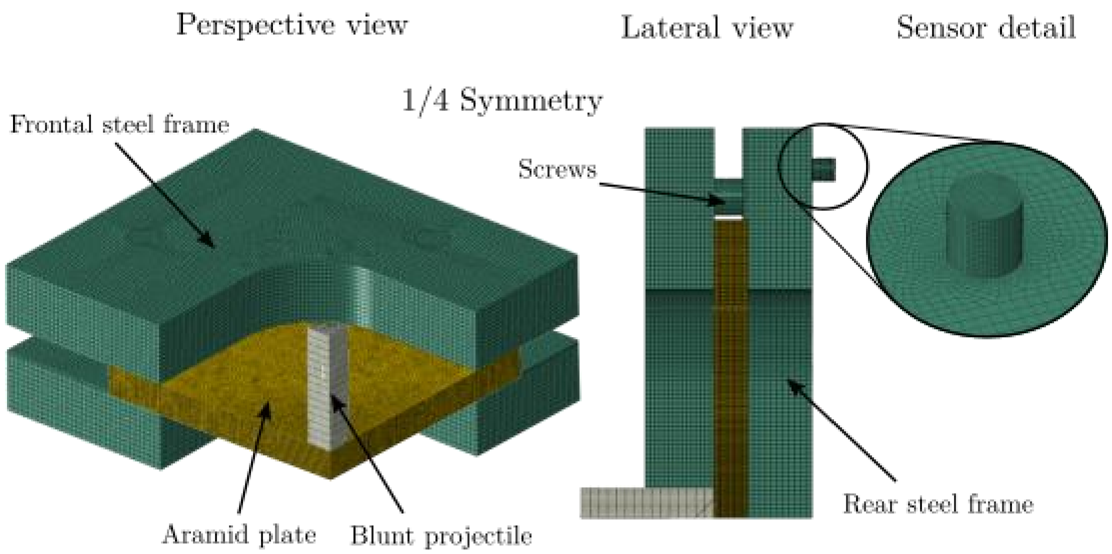

Figure 6. FEM model developed for impact test.

The contact between the plate and projectile and streel frames is defined with penalty contact algorithm and hard contact model [18]. The "hard contact" model allows adjusting the stiffness generated by the "penalty contact algorithm" to minimise penetration without adversely affecting the time increment. Concerning friction, a frictional coefficient equal to $\mu = 0.2$ is assumed. This is a typical value used in aramid impact problems [17,29].

4. Experimental and numerical results

The numerical model was validated comparing with experimental results. Subsequently, an analysis of the influence of the projectile mass (m_p) on the impact of aramid plates is carried out.

A total of 6 tests are performed at different initial impact velocities (V_0) in the range of 98 m/s to 174 m/s (*non-perforation configuration*) to validate the numerical model presented in this work. In each test, the resistance force is measured through the piezoelectric sensors. Then, remarkable damage is first observed by visual inspection of the specimens. Finally, permanent back-face deformation is measured using the profilometer to obtain the residual deformation generated due to different initial impact velocities.

4.1. Resistance force vs Impact velocity analysis

Figure 7 shows the results between the experimental test and numerical simulations for impact forces. Six experimental tests are performed within a range of impact velocities, from 98 m/s to 178 m/s.

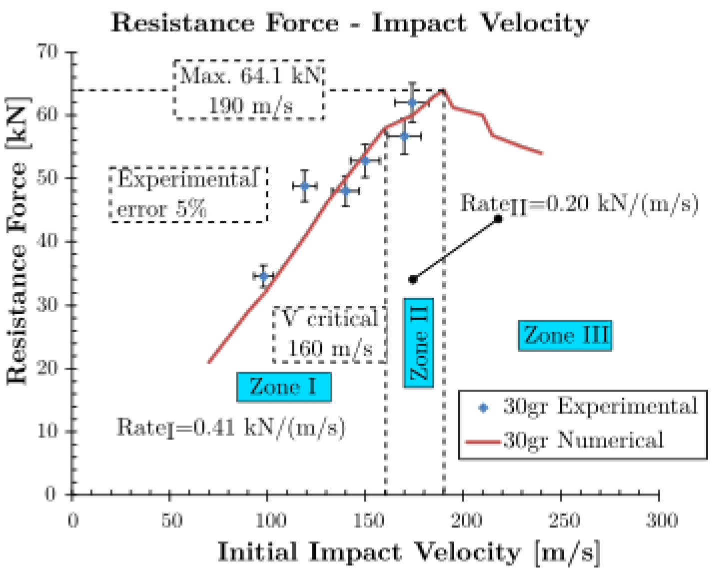

Figure 7. Resistance force comparison between experimental and numerical results.

It can be observed that the numerical model provides a good correlation with experiments. Three zones are observed in Figure 7. In zone I, with a rate (Force/Impact velocity) of *0.41 kN/(m/s)*, both the experimental and numerical impact force show a increasing linear trend with impact velocity. A transition region (zone II) is found between 160 m/s and 190 m/s because the first few layers of the laminate are broken. In this zone the rate decreases by half, *0.20 kN/(m/s)*. This zone is delimited by the maximum peak force, *64.1 kN*, for an impact velocity of *190 m/s*. Over this impact velocity, a decreasing resistance force is observed (zone III).

4.2. Permanent Back Face Deformation (PBFD)

The permanent Back Face Deformation (PBFD), after the spring back effect, is brought along the plate's permanent deformation due to the absorption of elastic strain energy. PFBD is obtained using the profilometer device described previously. A comparison of the PBFD between experiments and numerical results is shown in Figure 8. A critical impact velocity is found at 70 m/s which corresponds to non-PBFD observation because the impact energy is dissipated by the cohesive interlayer damage. Above 70 m/s, a linear correlation between PBFD and the initial impact velocity is observed.

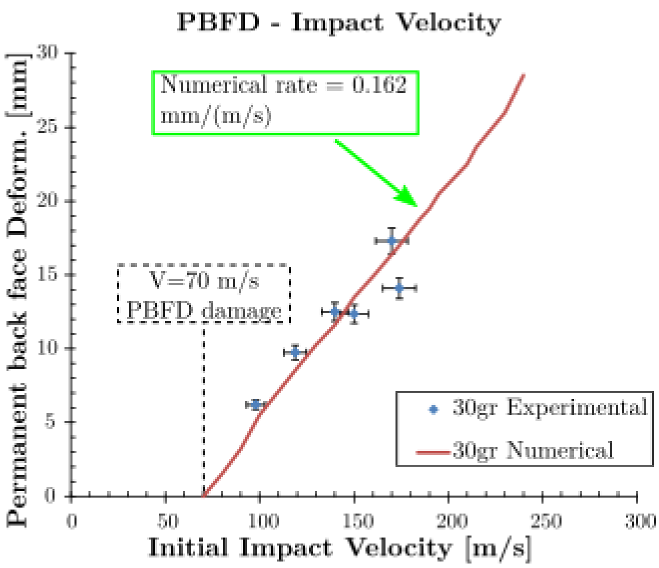

Figure 8. PBFD comparison between experimental and numerical results.

With a focus on analysing the external aspect of samples after impact, shrinkage phenomenon is caused, especially for high impact velocities. For illustrative purposes, experimental and numerical post-mortem specimens for 174 m/s are shown in Figure 9. The shrinkage, delamination and failure of the fibres are the main mechanisms that can be observed. The shrinkage mechanism is more noteworthy as the impact velocity increases.

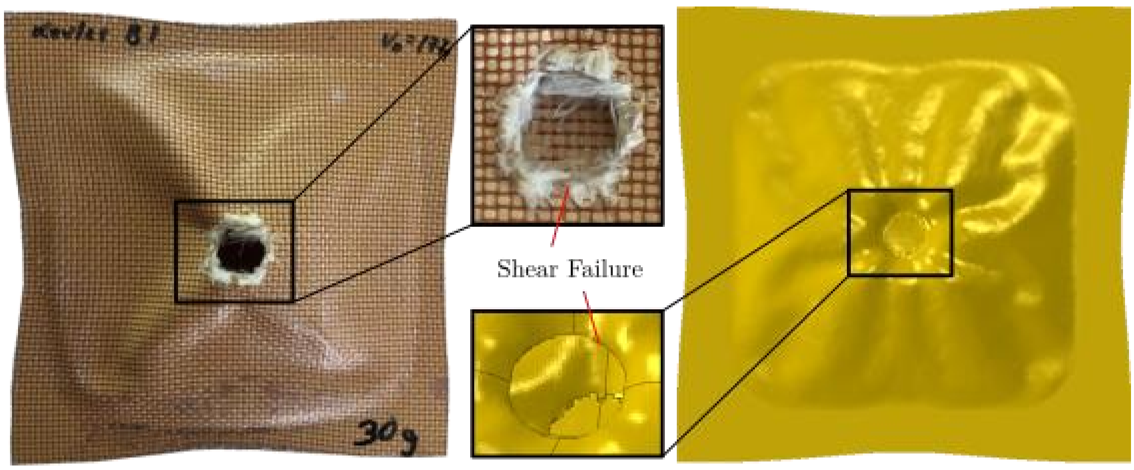

Figure 9. Qualitative comparison (experimental and numerical) of shrinkage and damage induced on samples.

The experimental data are summarized in the Table 4.

Impact velocity *[m/s]*	*Impact energy* *[J]*	*Resistance Force* *[kN]*	*PBFD* *[mm]*
98	144.06	34.5	6.2
119	212.415	48.8	9.74
140	294	48	12.5
150	337.5	52.8	12.35
170	433.5	56.68	17.31
174	454.14	62	14.1

Table 4. Resume of experimental test carried out.

4.3. Failure mechanisms and experimental observations

Computerized tomography allows to observe internal damage in tested samples with high quality without the need to break them. The specimen is focused on the impact zone to observe the local damage produced. Quantifying the delaminated surface is complex using this technique if the complete specimen is not analysed. However, on visual inspection it has been observed that the most relevant damage occurs at high impact velocities where failure of the first layers of the material occurs. At low impact velocities (~ 100 m/s), damage is limited to the local indentations in the impact zone.

For this reason, the computed tomography tool helps analysing the morphology of the damage induced in the specimen. The CT tests were carried out at the LEM3 of the University of Loraine. Figure 10 shows a comparison between the experimental specimen using this technique and the same numerical case for the most critical case analysed, impact velocity equal to 174 m/s. A good correlation is observed between results observed during experiments and numerical models, which correctly reproduces the failure modes and the final shape of plates after impact. In the impact zone, a through-thickness compaction layer occurs due to the nose shape projectile. Around this area, delamination increase being more notable at first layers, where shear failure is produced.

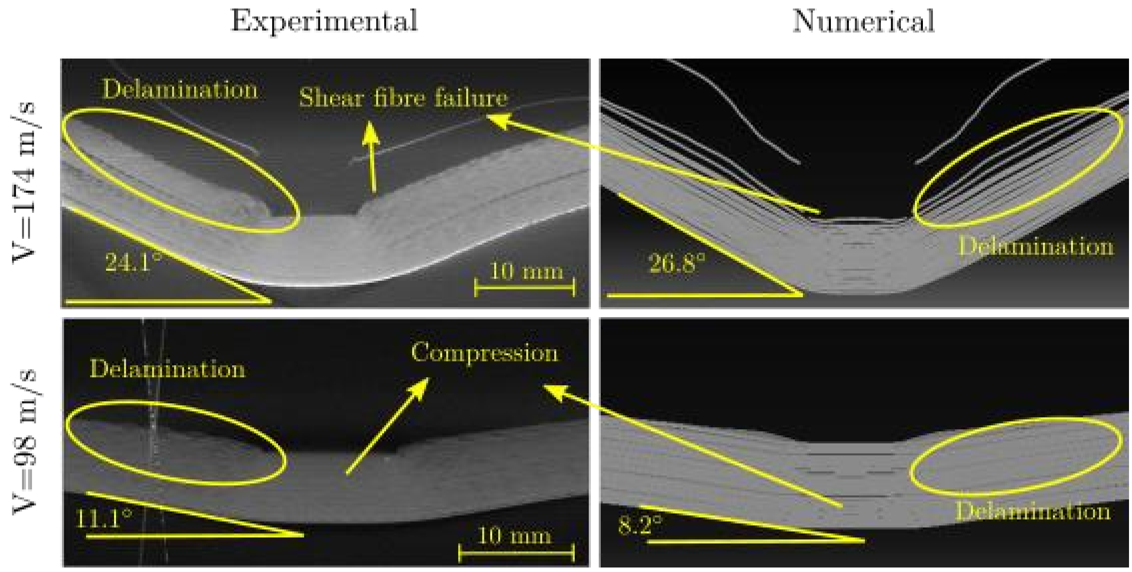

Figure 10. Failure mechanisms after impact using CT

4.4. Energy balance based on numerical simulations.

The internal mechanisms involve different absorption energies that can play relevant roles during the impact. For the sake of analysing the energy balance, only the numerical model can be used. Thus, the total balance energy total of the composite is based on the internal energy, the projectile kinetic energy, and other dissipated energies like frictions. The most important term of the composite plate is the internal energy, which is directly related to elastic energy, cohesive energy, and artificial energy. The energy balance is expressed as follows (Eq. 6-7):

$$E_{total} = E_{impact} = E_{inter} + E_{kin} + E_{dissip} \qquad 6)$$

where

$$E_{inter} = E_{elastic} + E_{cohesiv} + E_{artif} \qquad 7)$$

Figure 11a shows the energy balance for all impact cases where the energy absorbed by the cohesive damage, the internal energy, the elastic energy, and the artificial strain energy are plotted.

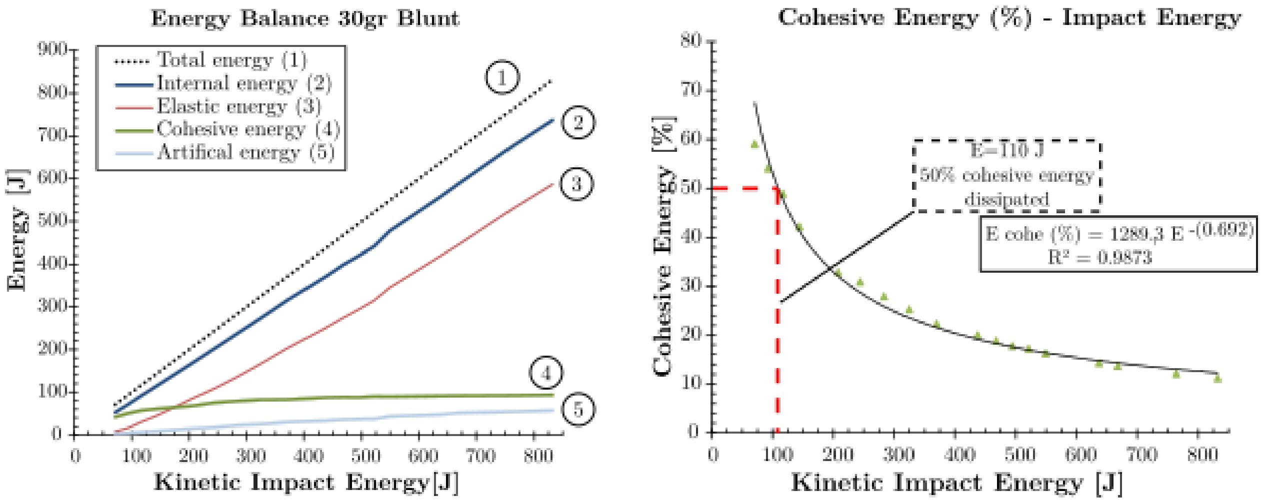

(a) (b)

Figure 11. The energy dissipated by damage related to impact energy. a) Complete energy balance. b) Cohesive energy study.

Increasing energies are observed with the impact energy except for the energy absorbed by the cohesive and artificial energy, which remains steady. These energies are associated with the different global and local mechanisms that appear with impact velocity. Focusing on the cohesive energy, the energy dissipated through the plate delamination decreases asymptotically as the impact velocity increases, as shown in Figure 11b.

The data shown in the figures of the numerical model are summarized in Table 5.

Impact Velocity [m/s]	*Impact Energy [J]*	*Resistance Force [kN]*	*PBFD [mm]*	*Absorbed Energy [J]*	*Artificial Energy [J]*	*Elastic Energy [J]*	*Cohesive energy [J]*	*Damage area (mm^2)*
26.00	10.00	14.00	0.00	5.20	0.27	0.32	4.68	178.38
70.00	70.81	21.00	0.00	52.58	2.76	8.01	41.81	6131.91
80.00	92.48	25.00	1.50	70.58	4.16	16.35	50.06	6694.50
90.00	117.05	29.00	3.20	92.00	6.80	31.00	57.20	7562.96
100.00	144.50	32.50	5.50	115.92	9.42	45.61	60.92	8342.97
120.00	208.08	41.20	8.70	170.54	15.40	86.68	68.30	9125.70
130.00	244.21	46.00	10.26	202.39	18.33	108.67	75.30	9280.84
140.00	283.22	50.00	11.60	236.95	22.79	135.20	78.94	9435.98
150.00	325.13	54.00	13.50	274.32	25.34	166.83	82.10	9713.82
160.00	369.92	58.00	14.90	315.01	30.16	202.41	82.40	9912.21
174.00	437.49	60.00	17.00	371.32	33.16	250.74	87.54	10386.82
180.00	468.18	61.60	18.00	398.72	35.57	275.11	87.99	10543.04
185.00	494.55	63.00	18.80	419.19	36.98	294.31	87.90	10530.07

190.00	521.65	64.00	19.50	441.84	37.33	315.16	89.55	10654.39
195.00	549.46	61.20	20.50	478.21	43.32	345.53	89.48	11179.28
210.00	637.25	60.00	22.50	557.42	47.32	419.11	91.08	11537.67
215.00	667.95	56.80	23.70	587.38	51.32	444.72	91.41	11822.54
230.00	764.41	55.00	26.00	678.00	54.20	531.00	92.30	11881.46
240.00	832.32	54.00	28.50	737.10	56.94	587.02	93.25	12083.63
250.00	903.13	53.00	31.00	806.86	61.35	649.64	95.97	12379.31

Table 5. Resume of numerical simulation developed.

According to the results of Table 5, the relationship between the damaged area and the impact energy can be expressed as:

$$Damage\ area\ (mm^2) = -4.068 \cdot 10^4 \times Impact\ Energy(J)^{-0.1031} + 3.231 \cdot 10^4 \quad (7)$$

the good agreement between numerical results and their fit is illustrated in Figure 12.

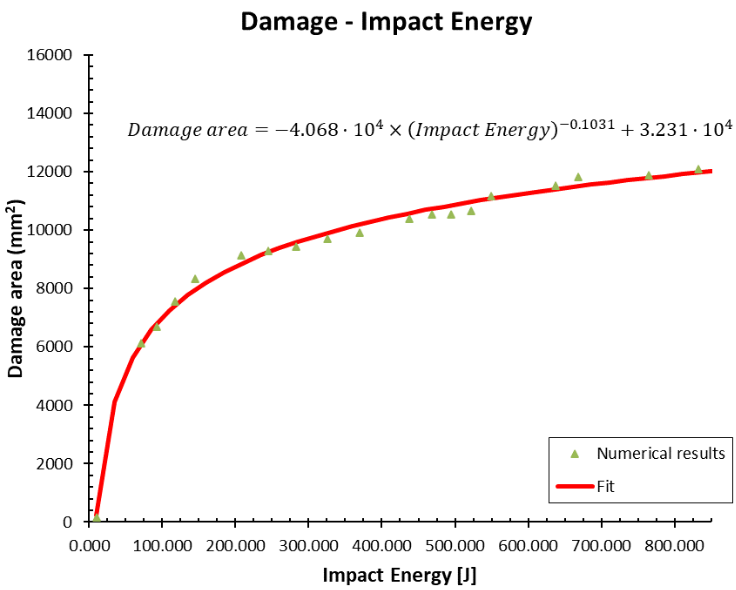

Figure 12. Damage area evolution with the impact energy.

4.5. Analysis of the influence of projectile mass

Since the numerical model provides accurate data with the experimental results because it has been calibrated and validated, the numerical model is used to analyse the effect of the mass impactor on the resistance force and PFBD, keeping the projectile diameter at different impact velocities. Two additional impactor masses are used: 20 g and 10 g.

Figure 13a provides information about the influence of impactor masses on the resistance force. All curves show a similar pattern over the impact energy. The change from zone I to zone II occurs at different impact energies; however, it is fair to point out that it is found at the same impact velocity, 160 m/s. The peak resistance force is reached at different impact energy and velocities. The maximum values are 56 kN and 46 kN for 20 g projectile and 10 g projectile, respectively. Figure 13b shows a linear trend between peak resistance force and projectile mass in the range of impact energy studied.

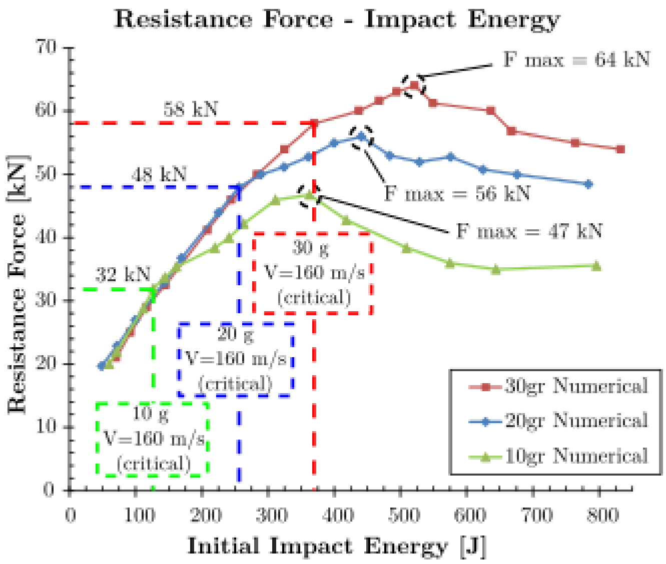

(a)

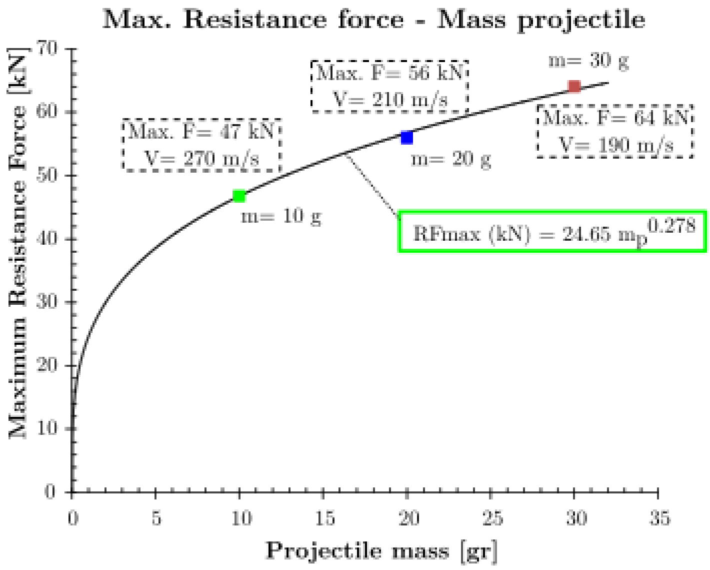

b)

Figure 13. Numerical mass influence analysis on resistance force. a) Resistance force vs Impact energy based on projectile mass influence b) Mass projectile influence on maximum resistance force.

The influence of impactor mass for the same projectile's diameters on PBFD could be interesting for manufacturers and armour designers. According to our results, the impactor length/weight ratio has no influence on PBFD for the same impact energy, Figure 14.

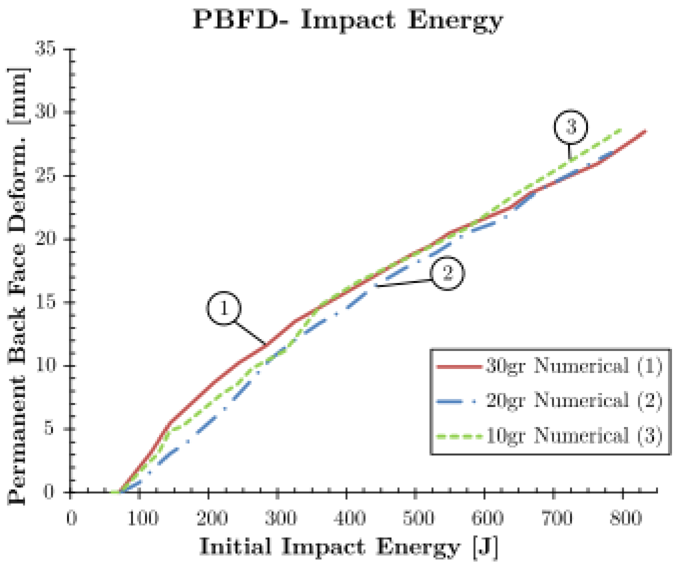

Figure 14. Permanent back face displacement for different projectile masses impacted.

5. Discussion

This paper presents a numerical model to predict the mechanical behaviour of aramid/PVB laminates for non-perforated impacts. The study has been carried out using a blunt projectile. The ballistic analysis of an impact structure should not be linked only to the ballistic limit, i.e. whether the projectile passes through the armour. Numerous parameters that are essential for the design of this type of structure for non-perforating operations should be analysed.

The relationship of the impact resistance to the failure mechanisms and the permanent deformation of the plate provide relevant information. It has been observed that before breaking the first layers of the material, delamination is the predominant energy absorption mechanism, leading to large deformation of the specimen. However, at high impact velocities, a more significant breakage of fibres is observed, and thus, the stiffness decreases and an increase of PFBD is found. This statement may be linked to the increase in plate shrinkage at high speeds. As it is shown in Figure 11a, at high impact velocities, the elastic energy (associated with the deformation of the plate and breakage of fibres) is the system's primary energy since the energy absorbed by the cohesive is almost constant. For impact velocities below the critical velocity ($v_o = 160\ m/s\ or\ E_{impact} = 384\ J$), the importance of the energy absorbed by the cohesive is 22% of the total. However, when PFBD is measured ($v_o =\ 70\ m/s$), the energy absorbed by the cohesive is practically 60%, according to Figure 11b, where fibre breakage does not occur. For impact velocities above 90 m/s, the elastic energy increases and becomes the system's main energy, leading to an increase in the PFBD.

Regarding the influence of mass, the maximum resistance is linearly related to the impact energy; the highest energy is given to the highest mass impactor. However, the breakage of the first layer of the laminate is linked to the same impact velocity. PBFD is independent of the mass of the projectile for the same impact energy.

6. Conclusions

This paper has developed a combined experimental and numerical methodology to analyse the impact force and permanent back face deformation on aramid/PVB composite plates. The paper's main contribution is the analysis of aramid composite behaviour and energy absorption mechanisms under high energy impact on a non-perforation regime.

An experimental test campaign involving instrumentation of the process to obtain the impact velocity of the projectile and impact force history on the target plate during the impact event was carried out. An interesting parameter on the structures' design is the permanent back face deformation (PBFD) which has been measured using a digital profilometer, and a significant dependency with impact velocity was observed.

The numerical model is based on the Hou modified criterion, and it has been implemented in a user subroutine to be used with the finite element code ABAQUS. The laminate is modelled with the same number of layers as specimens considering the cohesive surface between layers. The present numerical model successfully predicts aramid/PVB laminates' mechanical behaviour using blunt projectiles for impacts.

From the failure of the specimens, it has been observed that hardly any penetration occurs in the range of the initial impact velocities considered and that most of the impact energy is absorbed through the deformation of the specimen. The delamination originates this deformation between layers that allows its relative displacement, causing a decrease in the specimen's stiffness and, therefore, greater ease of deformation. From this deduction, it can be stated that by increasing the impact energy in the study range, where the penetration is shallow, and no complete perforation is achieved, and affecting only the first layers of the composite, the permanent deformation of the back-face deformation of the plates increases linearly. This statement has been corroborated with the numerical model developed, yielding a good correlation between both results.

Furthermore, it has been observed how the amount of energy dissipated by the delamination between layers of the composite decreases as the impact energy increases, going from a more global response of the system where this failure mechanism is the majority concerning others such as the breakage of fibres or crushing, to more localised damage, where this type of failure is representative.

Acknowledgements

The authors acknowledge the Ministry of Economy and Competitiveness of Spain and FEDER program under the Project DPI2017-88166-R for the financial support of the work. Prof. A. Rusinek acknowledges the financial support from the program UC3M-Santander Chair of Excellence in additive manufacturing.

References

1. Bhatnagar, A.; Institute of Materials, M. Lightweight ballistic composites : military and law-enforcement applications; CRC Press, **2006**; ISBN 0849391199.

2. US Dept of Justice. Nij 0106-01 (National Institute of Justice) Standard for Ballistic Helmets, 1981.

3. Tan, V.B.C.; Lim, C.T.; Cheong, C.H. Perforation of high-strength fabric by projectiles of different geometry; International Journal of Impact Engineering **2003**; 28; 207-222.

4. Bresciani, L.M.; Manes, A.; Ruggiero, A.; Iannitti, G.; Giglio, M. Experimental tests and numerical modelling of ballistic impacts against Kevlar 29 plain-woven fabrics with an epoxy matrix: Macro-homogeneous and Meso-heterogeneous approaches. Compos. Part B Eng. 2016, 88, 114–130, doi:10.1016/j.compositesb.**2015**.10.039.

5. Li, X.; Nia, A.B.; Ma, X.; Yahya, M.Y.; Wang, Z. Dynamic Response of Kevlar ®29/Epoxy Laminates under Projectile Impact-Experimental Investigation. Mech. Adv. Mater. Struct. ISSN **2017**, 24, 114–121, doi:10.1080/15376494.2015.1107670.

6. Wang, Y.B.; Wang, X.J.; Hu, X.Z; Sun,Y.X. Experimental study on penetration and perforation of laminated kevlar. Journal of Beijing Institute of Technology, **2004**, 13(3):317–323.

7. Sikarwar, R. S.; Velmurugan, R.; Madhu, V. Experimental and analytical study of high velocity impact on Kevlar/Epoxy composite plates. Central European Journal of Engineering,**2012**, 2(4), 638-649.

8. Van Hoof, J. Modelling of Impact Induced Delamination in Composite Materials; Carlenton University: Ottawa, ON, Canada, **1999**.

9. Palta, E.; Fang, H.; Weggel, D.C. Finite element analysis of the Advanced Combat Helmet under various ballistic impacts. Int. J. Impact Eng. **2018**, 112, 125–143, doi:10.1016/j.ijimpeng.2017.10.010.

10. Tham, C.Y.; Tan, V.B.C.; Lee, H.P. Ballistic impact of a KEVLAR® helmet: Experiment and simulations. Int. J. Impact Eng. **2008**, 35, 304–318, doi:10.1016/j.ijimpeng.2007.03.008.

11. Moure, M.M.; Rubio, I.; Aranda-Ruiz, J.; Loya, J.A.; Rodríguez-Millán, M. Analysis of impact energy absorption by lightweight aramid structures. Compos. Struct. **2018**, 203, 917–926

12. Guoqi, Z.; Goldsmith, W.; Dharan, C.H. Penetration of laminated Kevlar by projectiles—I. Experimental investigation. Int. J. Solids Struct. **1992**, 29, 399–420

13. Karahan, M.; Jabbar, A.; Karahan, N. Ballistic impact behavior of the aramid and ultra-high molecular weight polyethylene composites. J. Reinf. Plast. Compos. **2014**, 34, 37–48.

14. Liu, L., Cai, M., Liu, X., Zhao, Z.;Chen, W. Ballistic impact performance of multi-phase STF-impregnated Kevlar fabrics in aero-engine containment. Thin-Walled Structures, **2020**, 157, 107103.

15. Liu, L., Yang, Z., Liu, X., Chen, W., Zhao, Z.; Luo, G. Yarn dynamic tensile behavior and meso-scale numerical simulation method for STF-Kevlar fabrics. Thin-Walled Structures, **2021**,159, 107319.

16. Tan, L. Bin; Tse, K.M.; Lee, H.P.; Tan, V.B.C.; Lim, S.P. Performance of an advanced combat helmet with different interior cushioning systems in ballistic impact: Experiments and finite element simulations. Int. J. Impact Eng. **2012**, 50, 99–112, doi:10.1016/j.ijimpeng.2012.06.003.

17. Rubio, I.; Rodríguez-Millán, M.; Marco, M.; Olmedo, A.; Loya, J.A. Ballistic performance of aramid composite combat helmet for protection against small projectiles. Compos. Struct. **2019**, 226,

111153, doi:10.1016/j.compstruct.2019.111153.

18. Rubio, I.; Díaz-Álvarez, A.; Bernier, R.; Rusinek, A.; Loya, J.A.; Miguelez, M.H.; Rodríguez-Millán, M. Postmortem analysis using different sensors and technologies on aramid composites samples after ballistic impact. Sensors (Switzerland) **2020**, 20, doi:10.3390/s20102853.
19. Samal S, Marvalova B, Petrikova I, Vallons KAM, Lomov SV, Impact and post impact behavior of fabric reinforced geopolymer composite. Construction and Building Materials 2016; 127: 111-124, doi: 10.1016/j.conbuildmat.2016.09.145
20. Samal S, Reichmann D, Petrikova I, Marvalova B,. Low Velocity Impact on Fiber Reinforced Geocomposites. Applied Mechanics and Materials, 2016, 827, 145–148, doi: 10.4028/www.scientific.net/amm.827.145.
21. Rodriguez-Millan M, Garcia-Gonzalez D, Rusinek A, Abed F, Arias A. Perforation mechanics of 2024 aluminium protective plates subjected to impact by different nose shapes of projectiles. Thin-Walled Struct 2018;123:1–10. doi:10.1016/j.tws.**2017**.11.004.
22. Zhong, W.Z.; Mbarek, I.A.; Rusinek, A.; Bernier, R.; Jankowiak, T.; Sutter, G. Development of an experimental set-up for dynamic force measurements during impact and perforation, coupling to numerical simulations. Int. J. Impact Eng. **2016**, 91, 102–115, doi:10.1016/j.ijimpeng.2016.01.006.
23. Mbarek, I. A., Boumbimba, R. M., Rusinek, A., Voyiadjis, G. Z., Gerard, P.,Amadi-Dooki, A. The dynamic behavior of poly (methyl methacrylate) based nano-rubbers subjected to impact and perforation: Experimental investigations. Mechanics of Materials, **2018**, 122, 9-25.
24. Li, X.G.; Gao, X.L.; Kleiven, S. Behind helmet blunt trauma induced by ballistic impact: A computational model. Int. J. Impact Eng. **2016**, 91, 56–67, doi:10.1016/j.ijimpeng.2015.12.010.
25. Lee, H.P.; Gong, S.W. Finite element analysis for the evaluation of protective functions of helmets against ballistic impact. Comput. Methods Biomech. Biomed. Engin. 2010, 13, 537–550.
26. Moure-guardiola, C.; Rubio, I.; Antona-makoshi, J.; Olmedo, Á.; Loya, J.A.; Millán, M.R. Evaluation of Combat Helmet Behavior under Blunt Impact. Appl. Sci. **2020**, 1–22, doi:10.3390/app10238470.
27. Hou, J.P.; Petrinic, N.; Ruiz, C.; Hallett, S.R. Prediction of impact damage in composite plates. Compos. Sci. Technol. **2000**, 60, 273–281, doi:10.1016/S0266-3538(99)00126-8.
28. Gower, H.L.; Cronin, D.S.; Plumtree, A. Ballistic impact response of laminated composite panels. Int. J. Impact Eng. **2008**, 35, 1000–1008, doi:10.1016/j.ijimpeng.2007.07.007.
29. Rodríguez Millán M, Moreno CE, Marco M, Santiuste C, Miguélez H. Numerical analysis of the ballistic behaviour of Kevlar® composite under impact of double-nosed stepped cylindrical projectiles. J Reinf Plast Compos **2015**;35:124–37. doi:10.1177/0731684415608004.